
Article:
Alanazi, N. and Susmel, L. orcid.org/0000-0001-7753-9176 (2020) Estimating static/dynamic strength of notched unreinforced concrete under mixed-mode I/II loading. Engineering Fracture Mechanics, 240. 107329. ISSN 0013-7944

https://doi.org/10.1016/j.engfracmech.2020.107329

Estimating Static/Dynamic Strength of Notched Unreinforced Concrete under Mixed-Mode I/II Loading

N. Alanazi and L. Susmel
Department of Civil and Structural Engineering, The University of Sheffield, Mappin Street, Sheffield, S1 3JD, United Kingdom

Corresponding Author: Prof. Luca Susmel
Department of Civil and Structural Engineering
The University of Sheffield, Mappin Street, Sheffield, S1 3JD, UK
Telephone: +44 (0) 114 222 5073
Fax: +44 (0) 114 222 5700
E-mail: l.susmel@sheffield.ac.uk

Abstract

The Theory of Critical Distances (TCD) is a powerful design tool capable of estimating the strength of notched/cracked materials, with this being done by directly post-processing the linear-elastic stress fields ahead of the stress raisers being assessed. In the present study, an advanced formulation of the TCD is devised to specifically predict static and dynamic strength of notched unreinforced concrete subjected to Mixed-Mode I/II loading. The reliability and accuracy of the design approach being proposed was checked against a large number of experimental results generated by testing plain concrete containing notches of different sharpness, with these experiments being run not only under various degrees of Mode mixity, but also under different values of the nominal displacement rate (i.e., in the range 0.002-35 mm/s). The predictions made by this advanced version of the TCD were seen to fall mainly within an error interval of ±30%, that is, within an error band as wide as the band characterizing the intrinsic scattering of the calibration data. This suggests that that the TCD philosophy can effectively be extended also to the assessment of notched plain concrete subjected to in-service static/dynamic Mixed-Mode loading, with the relevant stress fields being determined by modelling concrete as a linear-elastic, homogeneous and isotropic material.

Keywords: Concrete, notch, critical distance, static loading, dynamic loading, mixed-mode I/II.

Nomenclature

3PB	three-point bending
4PB	four-point bending
a_f, b_f	material constants in the σ_f vs. $\dot{Z}$ relationship
$a_{K_{Id}}$, $b_{K_{Id}}$	material constants in the K_{Id} vs. $\dot{Z}$ relationship
a_L, b_L	material constants in the L vs. $\dot{Z}$ relationship
r_n	notch root radius
DIF	Dynamic Increase Factor
K_1	Mode I stress intensity factor
K_2	Mode II stress intensity factor
K_{Ic}	plane strain fracture toughness
K_{Id}	dynamic fracture toughness
$K_{t,b}$	stress concentration factor under pure bending
L	critical distance
Oxyz	system of coordinates
P	vertical load
$\dot{Z}$	reference dynamic variable
$\dot{Z}_{lower}$	value for $\dot{Z}$ defining the lower asymptotic limit
$\dot{Z}_{upper}$	value for $\dot{Z}$ defining the upper asymptotic limit
ε_p	local opening normal strain at the hot-spot
$\dot{\varepsilon}_p$	rate of the local opening normal strain at the hot spot
$\dot{\varepsilon}_{p,lower}$	value for $\dot{\varepsilon}_p$ defining the lower asymptotic limit
ρ	ratio between the Mode II and the Mode I stress intensity factor
σ_o	inherent strength
σ_{eff}	effective stress
σ_f	dynamic strength (i.e., failure stress under dynamic loading)
$\sigma_n(r)$	normal linear-elastic stress perpendicular to the focus path
σ_{nom}	nominal stress
σ_p	failure value of the local opening normal stress at the hot-spot
σ_y	normal stress parallel to axis y
σ_{UTS}	ultimate tensile strength
θ, r	polar coordinates
θ_c	angle defining the orientation of the focus path
θ_a	angle defining the orientation of the actual crack initiation plane
$\dot{\Delta}_c$	displacement rate parallel to the focus path
$\dot{\Delta}_{c,lower}$	value for $\dot{\Delta}_c$ defining the lower asymptotic limit

1. Introduction

As far as unreinforced concrete is concerned, most of the available design methods focus on modelling the mechanical behaviour/properties of cementitious materials by considering mainly the static problem. However, during their lifespan, real concrete structures can be damaged also by other events such as transient, time-variable, and dynamic loading, with the latter being due to, for instance, impact, crash, blast, or land sliding. This explain why, since the beginning of the last century, several attempts have been made also to establish a link between dynamic strength of cementitious materials and the rate of the applied loading [1-4]. In this context, examination of the state of the art shows that most of these studies were based on the so-called Dynamic Increase Factor (DIF). For a given mechanical property (such as, for instance, tensile strength or fracture toughness), the DIF is defined as the ratio between the value under the specific dynamic loading being considered over the corresponding value under quasi-static loading. This simple way of assessing the effect of rapidly increasing loading demonstrates that concrete materials can be very sensitive to the rate of the applied forces/moments. For instance, as far as strength is concerned, the associated DIF is seen to reach values larger than 2 under compression and way larger than 6 under tension [5]. However, despite this relatively large body of work, the available technical literature shows that, overall, the international scientific community has not yet agreed a commonly accepted approach suitable for assessing the strength of concrete under dynamic loading.

Concrete is made of coarse and fine aggregates bonded together via hydrated cement paste. As far as its mechanical response is concerned, concrete is usually treated as a brittle material, with this being done even though its incipient failure behaviour is always characterised by a certain level of plasticity/non-linearity [6].

The cracking processes being observed in concrete are very complex and difficult to anticipate because they depend on several factors that include, amongst others, water-to-cement ratio, characteristic of cement, type of aggregates, and curing protocol [7, 8]. Turning to the fracture mechanisms, cracks can originate either from pre-existing defects (i.e., the so-called

technological damage) or due to de-bonding between cement paste and aggregates [9, 10], with the latter being the prevailing failure process in situations of practical interest.

Due to the important role played by the fracture toughness, over the years specific experimental protocols have been developed to determine this classic mechanical property for concrete materials subjected to pure Mode I loading [11]. In parallel, systematic research work has been carried out also to measure the fracture toughness under Mode II loading as well as under Mixed-Mode I/II loading [12, 13]. In this context, different test arrangements have been proposed, optimised, and validated experimentally. Amongst the available solutions, certainly those methods making use of anti-symmetric four-point bending and single/double edge notches have rapidly gained popularity in industry. As far as these testing configurations are concerned, it is commonly believed that they can be used also to produce pure Mode II failures [14]. However, unfortunately, further studies [15-17] have demonstrated that under anti-symmetric four-point bending the crack propagation process can still be affected by secondary Mode I stress components even when the test is set-up to specifically investigate the fracture behaviour under pure Mode II loading.

While much theoretical and experimental work has been done to quantify and model the static/dynamic behaviour of unreinforced concrete, surprisingly, the detrimental effect of finite radius geometrical features (here termed notches) has so far received just little attention [18]. This lack of systematic research work is certainly surprising especially in light of the fact that, in the near future, additive manufacturing will bring into the concrete engineering discipline unprecedented design freedoms, with this allowing complex forms to be incorporated into innovative structural components [19]. From a strength point of view, the fact that concrete artefacts can contain complex geometrical features leads to localised stress concentration phenomena, the resulting stress gradients having a detrimental effect on the overall strength of the concrete parts themselves. Thus, effective and straightforward design methods need to be developed as a matter of urgency to allow engineers to effectively perform the static and dynamic assessment of concrete materials when they contain complex geometrical features.

Given the context briefly summarised above, the present investigation aims at advancing our understanding of the static and dynamic assessment of notched un-reinforced concrete. This will be done by reformulating the Theory of Critical Distances (TCD) [20] to allow this design approach to be employed also to estimate the strength of unreinforced concrete containing notches of different sharpness and subjected to static/dynamic Mixed-Mode I/II loading. The reliability and accuracy of this novel reformulation of the TCD will be checked against a large number of experimental results generated in the Sheffield Structures Laboratory by testing notched concrete beams under different degrees of Mode mixity as well as under different values of the displacement rate.

2. Fundamentals of the TCD under Mode I static loading

According to the TCD [20], an engineering material weakened by a stress raiser will withstand the static loadings being applied as long as the following condition is satisfied [20-22]:

$$\sigma_{eff} < \sigma_0 \tag{1}$$

In the above strict inequality σ_o is the inherent material strength, whereas σ_{eff} is the TCD effective stress calculated by post-processing the linear-elastic stress field acting on the material in the vicinity of the geometrical feature under consideration. Much experimental evidence demonstrates that, as far as brittle or quasi-brittle materials are concerned, σ_o can be taken invariably equal to the ultimate tensile strength, σ_{UTS} [22-24]. In contrast, σ_o is seen to be larger than σ_{UTS} for those material whose final breakage is preceded by a certain amount of plastic deformation [25-27]. Accordingly, for those material for which σ_o is larger than σ_{UTS}, the only way to determine the inherent strength is by running appropriate experiments [21]. This experimental procedure will be explained below in detail.

Turning back to the effective stress, according to the TCD, σ_{eff} can be determined in different ways by simply changing the strategy being adopted to post-process the relevant linear-elastic stress fields. In this setting, the simplest way to calculate σ_{eff} is by taking it equal to the stress

at a certain distance from the notch apex [28]. This formalisation of the TCD is known as the Point Method (PM) [20]. Alternatively, σ_{eff} can be determined also by averaging the relevant stress over a line [29] and this formalisation of the TCD is usually referred to as the Line Method (LM) [29]. It is worth re-calling here that the TCD effective stress can also be determined by adopting more sophisticated definitions. For instance, σ_{eff} can be calculated by averaging the relevant stress over a semi-circular area centred at the notch tip [30]. This bi-dimensional formalisation of the TCD is usually referred to as the Area Method [20]. Alternatively, according to the Volume Method, σ_{eff} can also be calculated by averaging the linear-elastic stress over a hemisphere centred at the notch tip [31].

Focussing attention solely on the simplest formalisations of the TCD, according to the systems of coordinates as defined in Fig. 1a, the mathematical equations to be used to calculate under static loading the TCD Mode I effective stress in terms of the PM and LM can be written in explicit form as follows [20, 22]:

$$\sigma_{eff} = \sigma_y\left(\theta = 0, r = \frac{L}{2}\right) \text{ – Point Method (PM, Fig. 1b)} \quad (2)$$

$$\sigma_{eff} = \frac{1}{2L}\int_0^{2L} \sigma_y\,(\theta = 0, r)dr \text{ – Line Method (LM, Fig. 1c)} \quad (3)$$

In definitions (2) and (3) L is the material critical distance. As postulated by the TCD, this length is a property which is different for different materials, but its value does not depend on the specific profile of the stress raiser being assessed [20]. In this framework, L can be thought of as a length scale parameter modelling the underlying microstructure. This explains why its value is seen to be directly linked with the relevant size of the microstructural heterogeneity characterising the material under investigation [32, 33]. As far as unreinforced concrete is concerned, some experimental evidence suggests that L is of the order of the average inter-aggregate distance [18, 34].

Under Mode I quasi-static loading, L can be estimated via the following well-known definition [23, 24, 35]:

$$L = \frac{1}{\pi}\left(\frac{K_{Ic}}{\sigma_0}\right)^2 \quad (4)$$

where K_{Ic} is the plane stress fracture toughness and σ_0 is the material inherent strength.

As far brittle or quasi-brittle materials are concerned, once K_{Ic} is known, L can be estimated directly via Eq. (4) since for this type of materials σ_0 is invariably equal to σ_{UTS} [20]. In contrast, seeing that ductile materials are characterised by an inherent strength that is larger than the conventional ultimate tensile strength [21, 26], the only way to determine L for this type of materials is by post-processing the results generated by testing specimens containing notches of different sharpness. This alternative strategy to determine L - which is based on the PM - is explained in Fig. 2a. In particular, assume that, for the material of interest, the strength of a series of notched specimens is determined experimentally. In this context, the calibration results are to be generated by testing a set of samples containing a known blunt notch and another set of specimens weakened by a known sharp notch. As per Fig. 2a, the resulting linear-elastic stress fields can then be plotted together in the incipient failure condition. By so doing, the coordinates of the point at which these two stress-distance curves intersect each other return the value not only of inherent strength σ_0, but also of critical distance L (Fig. 2a). In this setting, it is interesting to observe that, when K_{Ic} is unknown, a similar strategy can be followed also to determine L for brittle materials, the advantage being that in this case just one type of notch is needed to estimate the critical distance. In particular, according to Fig. 2b, given the notch stress field distribution in the incipient failure condition, the distance at which the stress equals the material ultimate tensile stress allows distance L/2 to be estimated directly. These considerations suggest that the TCD can be used also as an alternative strategy to estimate the plane stress fracture toughness from experimental results generated by testing specimens containing known geometrical features [36].

This section briefly summarises the key features of the TCD when this powerful design approach is used to perform the static assessment of engineering materials containing stress

raisers of all kinds and subjected to Mode I loading. In the next section, by taking full advantage of the work we did in the recent past [18, 22, 26, 37, 38], the TCD will be generalised so that it can be used also to design notched unreinforced concrete subjected to in-service static/dynamic Mixed-Mode loading.

3. Assessing notch strength of concrete under static/dynamic Mixed-Mode loading

As briefly discussed in the previous section, the inherent material strength and the critical distance are two key material properties that are needed to apply the TCD.

As far as the inherent strength is concerned, since the mechanical response of unreinforced concrete under quasi-static loading can be modelled as being predominantly brittle [6], the hypothesis can be formed that, for cementitious materials as well, σ_0 is invariably equal to σ_{UTS}. This hypothesis can then be extended also to those situations involving dynamic loading [18]. In other words, the assumption can be made that, under dynamic forces and moments as well, the inherent material strength of unreinforced concrete can directly be taken equal to its dynamic strength, σ_f.

With regard to a suitable definition for σ_0, it is important to recall here that, in general, the flexural strength of engineering materials is seen to be larger than the corresponding strength under tensile loading. This phenomenon is particularly evident in concrete. As far as conventional engineering materials are concerned, much experimental evidence [20, 21] suggests that the TCD calibrated using the ultimate tensile stress is somehow capable of taking into account the increase in strength that is observed under bending. Unfortunately, when it comes to concrete, nothing definitive can be said about this aspect due to a lack of suitable experimental results. Thus, certainly, this point deserves to be investigated in detail in the future. Having considered this important aspect, in the present investigation we used the static and dynamic flexural strength to determine the inherent material strength because, as long as concrete is involved, bending is certainly one of the most relevant loading scenarios in situations of practical interest.

Focussing attention on σ_f, according to the large number of experimental results collected and re-analysed by Malvar and Crawford [5], the tensile dynamic strength of unreinforced concrete is seen to increase as the local strain rate increases. This monotonic trend can be modelled by employing two simple power laws [5, 18], with an evident change in the exponent occurring as the strain rate approaches 1 mm/mm·s^{-1} [5]. Similarly, the dynamic fracture toughness as well is seen to increase linearly (in a log-log schematisation) as the local strain rate increases [39, 40]. Again, also for the dynamic fracture toughness a change in the slope is observed as soon as the local strain rate becomes larger than 1 mm/mm·s^{-1} [18].

If $\dot{Z}$ is used to denote either the loading rate, the displacement rate, the stress rate, the strain rate, or the stress intensity factor rate, the previous considerations can be generalised by assuming that the dynamic strength, $\sigma_f(\dot{Z})$, and the dynamic fracture toughness, $K_{Id}(\dot{Z})$, vary with $\dot{Z}$ according to the following power laws [18, 37]:

$$\sigma_0(\dot{Z}) = \sigma_f(\dot{Z}) = a_f \dot{Z}^{b_f} \tag{5}$$

$$K_{Id}(\dot{Z}) = a_{K_{Id}} \dot{Z}^{b_{K_{Id}}} \tag{6}$$

where a_f, b_f, $a_{K_{Id}}$, and $b_{K_{Id}}$ are material constants either to be determined experimentally or to be derived theoretically. It is worth observing here that relationships (5) and (6) must be defined so that they cover in a consistent way also the quasi-static case. In other words, Eqs (5) and (6) should be calibrated so that under quasi-static loading they return σ_{UTS} and K_{Ic}, respectively.

In more general terms, it is reasonable to expect that both Eq. (5) and Eq. (6) are characterised by a lower and an upper asymptotic limit (or plateau). Clearly, this aspect could be easily incorporated into the model by using more complex mathematical functions to define relationships $\sigma_0(\dot{Z})$ and $K_{Id}(\dot{Z})$. However, we do believe that this would make the model more complicated without resulting in any real improvement in terms of accuracy. Further, certainly using complex functions would result in more experimental work so that the required

calibration constants can be estimated accurately. In this context, it is important to observe that it is in any case very difficult to accurately define the values for $\dot{Z}$ delimiting the position of the asymptotic plateaus. For instance, under quasi-static bending, standard code EN 12390-5:2019 [41] recommends to select a constant rate of stress within the range 0.04 MPa/s (N/mm²·s) to 0.06 MPa/s (N/mm²·s). Further, a specific formula is provided to calculate the testing loading rate according to the size of the specimens and the distance between the lower rollers. Having highlighted this important aspect, certainly the simplest way to take into account the presence of the asymptotic plateaus is by simply limiting functions (5) and (6) as follows:

$$\sigma_0(\dot{Z}) \equiv \sigma_f(\dot{Z}_{lower}) \text{ and } K_{Id}(\dot{Z}) \equiv K_{Id}(\dot{Z}_{lower}) \qquad \text{for } \dot{Z} < \dot{Z}_{lower}$$

$$\sigma_0(\dot{Z}) \equiv \sigma_f(\dot{Z}_{upper}) \text{ and } K_{Id}(\dot{Z}) \equiv K_{Id}(\dot{Z}_{upper}) \qquad \text{for } \dot{Z} > \dot{Z}_{upper}$$

where $\dot{Z}_{lower}$ and $\dot{Z}_{upper}$ are used to determine the initial point of the lower and upper asymptotic plateau, respectively.

Having derived *ad hoc* expressions suitable for modelling strength and fracture toughness of unreinforced concrete under dynamic loading, the critical distance value is then proposed to be estimated as follows [18, 37]:

$$L(\dot{Z}) = \frac{1}{\pi}\left[\frac{K_{Id}(\dot{Z})}{\sigma_0(\dot{Z})}\right]^2 = a_L \dot{Z}^{b_L} \tag{7}$$

where a_L and b_L can directly be determined as soon as the calibration constants in relationships (5) and (6) are known.

It is important to recall here that, from a structural integrity viewpoint, critical distance L plays the role of a material length defining the size of that region (i.e., the so-called process zone) which controls the overall strength of the component being assessed [21, 22]. Accordingly, since the mechanical/fracture behaviour of concrete changes as the rate of the applied

loading/deformation varies [5], the size of the process zone (i.e., critical distance L) must vary with increasing of Ż so that these changes in terms of mechanical response and strength can be modelled accurately. In other words, definition (7) is used to create a link between the critical distance under quasi-static loading and the corresponding values under dynamic loading.

After extending to the dynamic case the definition of the inherent material strength, Eq. (5), as well as of the critical distance, Eq. (7), the subsequent step in the reasoning is establishing a simple rule suitable for determining under Mixed-Mode loading the orientation of the focus path that is needed to apply the TCD in the form of either the PM or the LM. To this end, the hypothesis can be formed that both initiation and initial propagation of static/dynamic cracks in unreinforced concrete are Mode I governed [7, 42]. Therefore, concrete is hypothesised to fail due to tensile cracks whose initial propagation occurs along those directions experiencing the maximum opening normal stress [22]. According to this simple assumption, the focus path to be used to apply the TCD can directly be taken coincident with a straight line emanating from the hot-spot (i.e., the assumed crack initiation site) and perpendicular to the surface at the hot-spot itself. In this specific context, the hot-spot is defined as that superficial point which experiences the maximum value of the opening normal stress – with the opening normal stress being tangential to the surface at the hot-spot and, therefore, coincident with the maximum principal stress. This definition suggests that, according to the opening normal stress-based damage model being adopted, the focus path is then assumed to be coincident with the crack initiation plane.

In order to better clarify the way the focus path is suggested as being determined under Mixed-Mode loading, consider the concrete notched beam loaded in combined bending and shear that is shown in Fig. 3a. Since the system of external forces/moments results in local Mixed-Mode stress distributions, the superficial point which is subjected to the maximum value of the maximum principal stress is no-longer coincident with the notch tip [43]. Accordingly, its exact location must be determined either by solving Finite Element (FE) models or by using suitable analytical solutions [44-46]. Having found the position of the location experiencing

the maximum opening normal stress, the focus path then is obtained by plotting a straight line that emanates from the hot-spot and is perpendicular to the surface at the hot-spot itself (Fig. 3a). In Fig. 3a the angle between the focus path and the notch bisector is denoted as θ_c.

Assume now that the notched beam under consideration is simply loaded in pure Mode I bending (Fig. 3b). According to the geometrical rule as defined above, under these specific circumstances the focus path invariably coincides with the notch bisector (i.e., θ_c=0°) since, obviously, the notch tip is now the point experiencing the maximum opening stress. This confirms that, as the general rule being proposed is adopted to address pure Mode I situations, it returns a focus path having the same orientation as the one recommended to be used to apply the TCD in its classic, standard form [20] – see Fig. 1.

Clearly, the simple rule being proposed above works well with finite radius stress concentrators. In contrast, it cannot be used to define the orientation of the focus path in the presence of stress raisers (i.e., either cracks or notches) that are modelled by taking the root radius invariably equal to zero. Under these circumstances, by using the LM argument, the focus path can then be taken coincident with a straight line emanating from the crack/notch tip and experiencing the maximum averaged value of the stress perpendicular to the line itself. This simple rule allows then the focus path to be defined unambiguously also in the presence of sharp geometrical features.

Having devised a set of simple rules to define origin and orientation of the focus path, the subsequent step is defining in a more rigorous way dynamic variable $\dot{Z}$ to be used along with Eqs (5) to (7). In particular, $\dot{Z}$ is proposed here to be calculated in terms of either the displacement rate, $\dot{\Delta}_c$, or the local opening normal strain rate at the hot spot, $\dot{\varepsilon}_p$. In this context, displacement rate $\dot{\Delta}_c$ will be use to check the accuracy of the TCD when a global, nominal quantity is used to define dynamic variable $\dot{Z}$. In contrast, since the strain rate is the most commonly adopted variable to model the behaviour of engineering materials under dynamic loading, $\dot{\varepsilon}_p$ will be employed to assess the accuracy of the PM and LM as they are applied along with a local quantity.

Turning back to the displacement rate, for the sake of consistency in the re-analyses discussed in what follows $\dot{\Delta}_c$ will be determined always along a direction that is parallel to the focus path – see Figs 3a and 3b. As far $\dot{\varepsilon}_p$ is concerned, this local quantities instead will be taken equal to the rate of the tangential (i.e., opening) normal strain at the hot-spot.

By making use of the definitions discussed in the previous sections, the TCD can now be reformulated consistently to be used to perform the static/dynamic assessment of notched unreinforced concrete under Mixed-Mode loading. In particular, initially, condition (1) has to be extended to the dynamic case (i.e., generalised) by assuming that failure takes place as soon as the TCD effective stress becomes equal to corresponding reference strength, i.e.:

$$\sigma_{\text{eff}}(\dot{Z}) = \sigma_0(\dot{Z}) \Leftrightarrow \text{failure} \tag{8}$$

where $\sigma_0(\dot{Z})$ is defined according to Eq. (5). Effective stress $\sigma_{\text{eff}}(\dot{Z})$ instead can directly be calculated according to the PM and the LM by re-writing definitions (2) and (3) as follows:

$$\sigma_{\text{eff}}(\dot{Z}) = \sigma_n\left(r = \frac{L(\dot{Z})}{2}\right) - \text{Point Method (PM)} \tag{9}$$

$$\sigma_{\text{eff}}(\dot{Z}) = \frac{1}{2L(\dot{Z})}\int_0^{2L(\dot{Z})} \sigma_n(r)dr - \text{Line Method (LM)} \tag{10}$$

where $\sigma_n(r)$ gives the distribution of the normal linear-elastic stress perpendicular to the focus path (Fig. 3), r is a rectilinear coordinate coincident with the focus path, and critical distance $L(\dot{Z})$ is determined according to Eq. (7).

As far as the calibration of the TCD is concerned, another important aspect that must be mentioned explicitly is the so-called volume effect. In particular, it is well-known that the overall strength of concrete is affected by the absolute volume of material under stress. Accordingly, given the actual dimensions of the structural detail aimed to be assessed, the size of the specimens to be used to determine the relevant material properties must be chosen according to the recommendations of the available standard codes. By so doing, the TCD

becomes safe to be used to perform static and dynamic assessment, with this holding true independently of the absolute dimensions of the component being designed.

Having reformulated the TCD to be used to assess static/dynamic strength of notched unreinforced concrete under Mixed-Mode loading, the next step is obviously checking the accuracy and reliability of the design approach being proposed against relevant experimental results. This will be done in what follows.

To conclude, it is worth pointing out that, as devised in the present section, the method being proposed can be used to model the role of macroscopic geometrical features. However, thanks to the unique features of the TCD, it is reasonable to believe that a similar methodology could be used also to assess the detrimental effect of manufacturing flaws, with this being done by taking into account their size, shape and location. To this end, the TCD should be re-formulated by addressing the problem either at a mesoscopic or at a microscopic level. In this setting, due to the important role played by manufacturing flaws in determining the overall strength and fracture behaviour of concrete materials, certainly this alternative way of using the TCD would deserve to be investigated systematically both from a theoretical and an experimental point of view.

4. Details of the experimental investigation

To investigate whether the proposed reformulation of the TCD is successful in estimating static/dynamic Mixed-Mode strength of notched unreinforced concrete, a large number of experimental results were generated in the Sheffield Structures Laboratory by testing, under symmetric and asymmetric bending, 100 mm x 100 mm square section beams having length equal to 500 mm. These beams were cast so that both the un-notched (Fig. 4a) and the notched specimens (Figs 4b and 4c) had net nominal width equal to 50 mm. The U-notched specimens were designed to investigate experimentally the detrimental effect of three different values of the root radius, r_n. As shown in Figs 4b and 4c, the blunt notches had root radius equal to 24 mm, with the resulting stress concentration factor under pure bending, $K_{t,b}$, being equal to

1.44. The intermediate notches had instead root radius equal to 12.5 mm ($K_{t,b}$=1.76), whereas for the sharp notches r_n was equal to 1.3 mm ($K_{t,b}$=4.51).

The blunt as well as the intermediate notches were manufactured by gluing plastic pipes (having outer diameter equal to 48 mm and to 25 mm, respectively) onto the bottom of the moulds. After curing, the pipes were removed by cutting out the concrete, so that the specimens could be tested with the region in the vicinity of the notch tip being in the as-cast condition. In contrast, the sharp notches were directly machined by making the crack-like slits with a circular saw having thickness equal to 2.6 mm.

Both the un-notched and the notched specimens were fabricated according to the standardised procedures recommended in Refs [47, 48]. In more detail, 30 N/mm^2 Portland cement was mixed with 10 mm graded natural round gravel and grade-M sand. The water-to-cement ratio was set equal to 0.44. Before casting the concrete mix, the moulds were internally coated with a release agent to allow the concrete beams to easily be demoulded without causing any damage to the specimens themselves. Both un-notched and notched samples were removed from the moulds 24 hours after casting and then cured and stored in a moist room. This procedure resulted in a concrete having under quasi-static loading the following mechanical properties: flexural strength equal to 5.8 MPa, compressive strength equal to 65 MPa and Young's modulus to 38 GPa.

Turning to the mechanical testing, the levels of Mode mixity being investigated were quantified via the ratio, ρ, between the Mode II (K_2) and the Mode I (K_1) stress intensity factor, i.e., $\rho=K_2/K_1$. In particular, ρ was determined analytically [49, 50] for all the load configurations being considered by simply replacing the notches in the specimens of Figs 4b and 4c with ideal zero-tip radius cracks having length equal to 50 mm.

The results under pure Mode I loading (ρ=0) were generated by using a standard symmetric three-point bending (3PB) set-up as shown in Fig. 5a. According to the testing configuration sketched in Fig. 5b, the same 3PB set-up was also used with the asymmetric specimens to generate results under a Mode mixity ratio, ρ, equal to 0.18. Finally, a series of experiments were run under asymmetric four-point bending (4PB). In particular, the testing set-up shown

in Fig. 5c was used to investigate the static/dynamic behaviour of the notched concrete specimens of Fig. 4b under a Mode mixity ratio, ρ, equal to 0.30.

As far as the un-notched specimens (Fig. 5a) are concerned, they were tested under three point bending, with the experimental set-up being optimised so that the cracks always initiated and propagated at the centre of the specimens themselves - i.e., away from the re-entrant corners. All the tests were run by employing a vertical hydraulic actuator. A pre-load of approximately 0.2 kN was always used to ensure that, before applying the ramp loading, the specimens were already in full contact with the cylindrical rollers. The magnitude of the force applied during testing was measured and then gathered using a high-precision dynamic loading cell that was attached to the end of the piston road of the hydraulic cylinder. The experimental results were generated by controlling the vertical movement of the piston road itself, with the nominal displacement rate ranging from about 0.002 mm/s to about 35 mm/s.

High-speed camera Phantom Miro 310 was used to double-check the synchronism between crack initiation process and recorded peak failure force as well as to measure the actual displacement rate being applied during testing. Furthermore, by taking full advantage of the Digital Image Correlation (DIC) technique, the camera was used also to measure the local displacements in the notch tip regions.

Synchronising the high-speed/high-resolution videos with the force vs. time signals gathered from the loading cell allowed us to fully confirm that the maximum force in the force vs. time curve always corresponded to the presence of a visible initiation crack on the surface of every specimen being tested. Accordingly, for each test, the maximum load gathered during testing was used to define the corresponding failure force. This was done being sure that neither the inertia of the piston road nor a possible delay in the signal gathered from the loading cell were affecting the post-processing of the experimental results.

5. Experimental results, cracking behaviour and focus path

The stress distributions in the tip regions of the notches being tested were determined by using commercial FE code ANSYS®. In the bi-dimensional models being solved numerically, the

concrete under investigation was assumed to behave like a linear-elastic, homogeneous and isotropic material. The notched samples shown in Figs 4b and 4c were modelled by using 4-node structural plane elements (plane 182), with the mesh density in the vicinity of the identified hot-spots being gradually increased until convergence occurred.

Initially, for any notch/loading configuration being investigated, the results from the FE analyses were used to determine the position of the hot-spots as well as the orientation of the corresponding focus paths. According to Section 3, the hot-spots were defined as those superficial points experiencing the maximum value of the tangential normal stress, with the focus paths being perpendicular to the surface at the hot-spots themselves. Given the different testing set-ups shown in Fig. 5, the directions of the focus path determined according to this simple rule were then used to calculate local displacement Δ_c via DIC – see Fig. 3 and Section 3 for the definition of Δ_c. Fig. 6 shows two examples of the forces and the corresponding DIC-measured displacements gathered under pure Mode I loading (Fig. 6a) as well as under Mixed-Mode I/II loading with ρ=0.3 (Fig. 6b). In these charts the directions of displacement Δ_c were determined according to the FE-based procedure discussed above.

The results generated by testing both the un-notched and the notched specimens are all summarised not only in Tables 1 to 4, but also in the semi-logarithmic diagrams seen in Fig. 7. In more detail, the chart of Fig. 7a reports the results obtained by testing the un-notched specimens under pure Mode I loading, with σ_f denoting the dynamic strength determined according to the beam theory in the incipient failure condition (i.e., under the maximum force recorded during testing). This graph makes it evident that the strength of the concrete being tested was characterised by an intrinsic level of scattering, with the experimental points falling within an error interval of ±30% [51]. However, the best-fit curved line based on a power law shown in Fig. 7a confirms that, as expected [5], the strength of the concrete being tested increased as the displacement rate, $\dot{\Delta}_c$, increased. The charts reported in Figs 7b to 7j summarise instead the experimental results that were generated by testing the notched specimens under Mode I as well as under Mixed-Mode I/II loading. In these graphs the strength, σ_p, is expressed in terms of tangential stress at the hot-spots determined, in the

incipient failure condition, from the FE models. Figs 7b to 7j confirm that, as expected, in the presence of stress raisers as well σ_p increased as $\dot{\Delta}_c$ increased, with the experimental data falling again within error bands of ±30%.

The pictures seen in Fig. 8 show some examples of the cracking behaviour that was observed in the notched concrete being tested under Mode I loading (Fig. 8a) as well as under Mixed-Mode I/II (Figs 8b and 8c). Independently of loading rate and Mode mixity, the direct inspection of all the fracture surfaces revealed that the cracks initiated in the highly-stressed regions mainly at the interfaces between matrix and aggregates, with the subsequent propagation taking place in the cement paste. The formation of these initial short tensile cracks was followed by an instable fracture process leading to the complete breakage of the specimens. In a number of cases, this fast, instable propagation resulted also in the breakage of some aggregates positioned away from the notch tip region.

Another interesting aspect that is worth considering here briefly is the effect in the notch regions of the three-dimensional stress constraint phenomenon. In particular, the specimens containing the crack-like notches (i.e., nominal notch root radius, r_n, equal to 1.3 mm) were characterised at a the mid-thickness section by a stress distribution that was very close to the one due to plane strain [52-54]. Accordingly, in the sharply notched specimens the stress state in the mid-thickness region was characterised by the largest degree of triaxiality, with this resulting in crack initiations mainly taking place at the mid-section. In contrast, for the other notches (i.e., specimens with r_n equal to 12.5 mm and 24 mm, respectively) the fact that the local constrain effect decreases as r_n increases resulted in initiations occurring also away from the mid-section, with the position of the crack initiation region being influenced more markedly also by the local material morphology.

The pictures on the left-hand side of Fig. 8 allow the observed crack paths to be compared directly with the directions of the focus path as determined numerically according to the rule stated in Section 3. These pictures confirm that, as expected, the cracks always initiated in the vicinity of those material hot-spots experiencing the largest value of the tangential normal stress. Further, the initial propagation was seen to occur predominantly along those directions

of maximum opening stress, with the TCD focus path as defined in Section 3 being clearly capable of locating the orientation of the crack initiation plane.

The accuracy and reliability in modelling the crack initiation process of the focus path as proposed to be defined in the present investigation is fully confirmed also by the graphs of Fig. 9. In more detail, these diagrams compare the theoretical value of angle θ_c as defined in Fig. 3 with the corresponding value, θ_a, directly measured on the surfaces of the broken specimens. These charts make it evident that the simple rule being proposed here to determine the orientation of the focus path is capable of capturing in a very accurate way the essence of the crack initiation process, with this holding true independently of Mode mixity and nominal displacement rate.

To conclude, it can be observed that, according to the charts of Fig. 9, the orientation of both the predicted and the experimentally measured crack initiation planes appears not to vary monotonically with ρ. To explain this trend, it is worth recalling here that ρ was defined as the ratio between K_2 and K_1, with stress intensity factors K_2 and K_1 being determined analytically [49, 50] by assuming that the specimens of Fig. 4 contained cracks having length equal to 50 mm and tip radius equal to zero. According to Fig. 5, a nominal Mode mixity ratio, ρ, of 0.18 was obtained by testing the notched specimens under symmetric 3PB, whereas a ρ value of 0.3 was obtained by testing the notched samples under asymmetric 4PB. The orientation of both the crack initiation planes and the focus paths were determined by defining angles θ_c and θ_a as seen in Fig. 3a. In order to clearly show the level of correlation between θ_c and θ_a in the charts of Fig. 9, the orientation for the crack initiation planes in the specimens tested under 3PB and under 4PB were measured on opposite lateral surfaces. This explains the reason why θ_c and θ_a are positive for ρ equal to 0.18, whereas they are negative for ρ equal to 0.30. In terms of absolute values of angles θ_c and θ_a instead, as expected, the orientation of the crack initiation planes tend to increase as ρ increases, with this holding true independently of the sharpness of the notch being tested.

6. Validation of the proposed reformulation of the PM and the LM

As briefly mentioned in Section 3, in order to check the accuracy of the PM, Eq. (9), and the LM, Eq. (10), in estimating the static and dynamic strength of the notched specimens being tested, variable Ż was defined by exploring two different strategies. In particular, Ż was taken either equal to the rate of the displacement parallel to the focus path, $\dot{\Delta}_c$ or equal to the rate of the opening normal strain determined at the hot spot, $\dot{\varepsilon}_p$. Accordingly, by post-processing the results obtained by testing the plain specimens under Mode I static/dynamic loading (Fig. 7a), it was straightforward to derive (via the standard least-squares method) the following values for constants a_f and b_f in Eq. (5):

$$\sigma_f(\dot{\Delta}_c) = 8.67 \cdot \dot{\Delta}_c^{0.071} \tag{11}$$

$$\sigma_f(\dot{\varepsilon}_p) = 14.58 \cdot \dot{\varepsilon}_p^{0.078} \tag{12}$$

The subsequent step was determining constants a_L and b_L in the L vs. Ż relationship, Eq. (7). This was done according to the methodology explained in Fig. 2b by post-processing the results from both the plain specimens and the sharply notched samples tested under Mode I loading (see Fig. 7d). By so doing, L was estimated for different values of either $\dot{\Delta}_c$ or $\dot{\varepsilon}_p$, obtaining:

$$L(\dot{\Delta}_c) = 4.7 \cdot \dot{\Delta}_c^{-0.03} \tag{13}$$

$$L(\dot{\varepsilon}_p) = 3.3 \cdot \dot{\varepsilon}_p^{-0.03} \tag{14}$$

It is important to highlight here that this simple and straightforward procedure allowed us to calibrate Eqs (11) to (14) so that, by setting $\dot{\Delta}_{c,lower}$=0.0035 mm/s or $\dot{\varepsilon}_{p,lower} = 7.4 \cdot 10^{-6}\ s^{-1}$, under quasi-static loading these functions return the values characterising the conventional mechanical behaviour. In contrast, owing to the fact that the experimental set-up being used

did not allowed us to explore the very-high loading rate regime, nothing can be said about the values for $\dot{\Delta}_c$ or $\dot{\varepsilon}_p$ that delimit the asymptotic upper limit.

Another important aspect that is worth pointing out here is that, according to Eqs (13) and (14), under quasi-static loading the critical distance value, L, was seen to approach 5.5 mm, with its value decreasing down to about 4.2 mm under the highest values of the loading rate that were explored. This suggests that, as observed in other related investigations [18, 34], also for the concrete being tested to generated the results summarised in Tabs 1 to 4, length L was seen to be of the order of the average inter-aggregate distance.

The reference strength quantified via Eqs (11) and (12) together with the critical distance expressed through Eqs (13) and (14) were then used to post-process all the results being generated in terms of the PM and the LM. To calculate the effective stress according to Eqs (9) and (10), the relevant stress fields were determined, in the incipient failure condition, by solving the linear-elastic FE models as briefly described at the beginning of Section 6.

Having calculated the TCD effective stress by taking dynamic variable $\dot{Z}$ equal to either $\dot{\Delta}_c$ or $\dot{\varepsilon}_p$, the accuracy of the predictions being made were assessed by adopting the following definition for the error:

$$\text{Error} = \frac{\sigma_{\text{eff}}(\dot{Z}) - \sigma_0(\dot{Z})}{\sigma_0(\dot{Z})} \times 100 \qquad (15)$$

This simple definition allowed us to check whether the reformulation of the TCD being proposed predicted failures conservatively or non-conservatively by assigning either positive or negative sign, respectively.

The overall accuracy obtained by applying the TCD in the form of the PM and the LM is summarised in the error diagrams of Figs 10. In particular, the charts of Figs 10a and 10c report the predictions made by considering the results generated under quasi-static loading. The diagrams seen in Figs 10b and 10d summarise instead the accuracy that was obtained when post-processing the results generated under dynamic loading. The charts of Fig. 10

demonstrate that the proposed approach was capable of accurately predicting the strength of the notched concrete being tested, with this holding true for the results generated both under Mode I and under Mixed-Mode I/II static/dynamic loading. In particular, as expected, a higher level of accuracy was achieved as taking dynamic variable Ż equal to $\dot{\varepsilon}_p$, i.e., when the TCD was applied along with a local quantity determined in the vicinity of the estimated crack initiation point.

To conclude, it is possible to observe that, in terms of overall accuracy, the level of scattering characterising the predictions being obtained is definitely adequate. This is because, according to Fig. 10, the systematic usage of the PM and LM returned estimates falling mainly within an error interval of ±30%, i.e., within a scatter band as wide as the scatter band characterising the two populations of data used for calibration (see Fig. 7a and 7d). This is certainly satisfactory since, by definition, a predictive method cannot return estimates that are less scattered than the population of data used to calibrate the method itself.

7. Conclusion

In the present investigation, a large number of notched samples were tested under static/dynamic Mixed-Mode loading in the Structures Laboratory of the University of Sheffield to investigate the strength of un-reinforced concrete weakened by stress concentrators of different sharpness. The TCD was reformulated in order to make it suitable for designing notched concrete against static/dynamic uniaxial/multiaxial loading. The accuracy and reliability of this alternative reformulation of TCD was checked against the results being generated. As per the outcomes from the research work summarised in the present paper, it is possible to draw the following key conclusions:

- the strength of concrete increases as the rate of the dynamic loading increases also in the presence of notches and under Mixed-Mode loading;
- the cracking behaviour of notched un-reinforced concrete is governed by the opening normal stress, with this holding true independently of degree of Mode mixity and rate of the applied displacement/loading;

- the focus path as recommended to be defined in the present investigation is seen to be capable of accurately predicting/modelling the orientation of the crack initiation planes;
- according to the TCD philosophy, for design purposes un-reinforced concrete can be modelled as a linear-elastic, homogenous, and isotropic material, with this resulting in a great simplification of the stress analysis problem;
- the linear-elastic TCD is seen to be successful in predicting the strength of notched un-reinforced concrete subjected to static/dynamic Mixed-Mode loading;
- the systematic use of the TCD applied in the form of the PM and the LM returned estimates falling mainly within an error band of ±30%, i.e. in estimates as scattered as the population of data used for calibration;

ACKNOWLEDGMENT

Support for this research work from the Engineering and Physical Sciences Research Council (EPSRC, UK) through the award of grant EP/S019650/1 is gratefully acknowledged. Nasser A. Alanazi is grateful to the University of Hail, Saudi Arabia, for sponsoring his PhD studentship. Thanks are also due to the Staff of the Sheffield Structures Laboratory who gave an invaluable support to perform all the experimental activities.

References

[1] Fu HC, Erki MA, Seckin M. Review of effects of loading rate on reinforced concrete. J Struct Eng 1991;117(12):3660-79.

[2] Fu HC, Erki MA, Seckin M. Review of Effects of Loading Rate on Concrete in Compression. J Struct Eng 1991;117(12):3645–3659.

[3] Bischoff PH, Perry SH, Compressive behaviour of concrete at high strain rates. Mater Struct 1991;24(6):425–450.

[4] Williams MS. Modelling of local impact effects on plain and reinforced concrete. ACI Struct J 1994;91(2)178–187.

[5] Malvar LJ, Crawford JE. Dynamic Increase Factors. Proceedings of the Twenty-Eighth DoD Explosives Safety Seminar, Orlando, Florida, 18-20 August, 1998.

[6] Neville AM, Brooks JJ. Concrete technology. Prentice Hall, USA, 2010.

[7] Anderson TL. Fracture mechanics: fundamentals and applications. CRC Press, Taylor & Francis Group, USA, 2005.

[8] Giaccio G, Zerbino AR. Failure Mechanism of Concrete: Combined Effects of Coarse Aggregates and Strength Level. Adv Cem Based Mater 1998;7(2):1998.

[9] Zhang B. Properties of Ordinary Concrete Under Bending Fatigue. Cem Concr Res 1998;28(5):699–711.

[10] Guo LP, Sun W, Zheng KR, Chen HJ, Liu B. Study on the flexural fatigue performance and fractal mechanism of concrete with high proportions of ground granulated blast-furnace slag. Cem Concr Res 2007;37(2):242–250.

[11] Karihaloo BL, Nallathambi P. Test Methods for Determining Mode I Fracture Toughness of Concrete. In: Shah S.P. (eds) Toughening Mechanisms in Quasi-Brittle Materials. NATO ASI Series (Series E: Applied Sciences), vol 195. Springer, Dordrecht, 1991,

[12] Swartz SE, Lu LW, Tang LD. Mixed-mode fracture toughness testing of concrete beams in three-point bending. Mater Struct 1988;(21):33–40.

[13] Swartz SE, Taha NM. Mixed mode crack propagation and fracture in concrete. Eng Fract Mech 1990;35(1–3):137–144.

[14] Bažant ZP, Pfeiffer PA. Shear fracture tests of concrete. Mater Struct 1986;19(2):111–121.

[15] John R, Shah SP. Mixed-Mode Fracture of Concrete Subjected to Impact Loading. J Struct Eng 1990;116(3):585-602.

[16] Reinhardt H, Xu S. Experimental determination of K_{IIC} of normal strength concrete. Mater Struct 1998;31:296–302.

[17] Carpiuc A. Innovative tests for characterizing mixed-mode fracture of concrete: from pre-defined to interactive and hybrid tests. PhD Thesis, University of Paris-Saclay, Paris, France, 2015

[18] Pelekis I, Susmel L. The Theory of Critical Distances to assess failure strength of notched plain concrete under static and dynamic loading. Eng Fail Anal 2017;82:378–389.

[19] Buswell RA, Leal de Silva WR, Jones SZ, Dirrenberger J. 3D printing using concrete extrusion: A roadmap for research. Cem Concr Res 2018;112:37-49

[20] Taylor D. The theory of critical distances: a new perspective in fracture mechanics. Elsevier, Oxford, UK, 2007.

[21] Susmel L, Taylor D. On the use of the Theory of Critical Distances to predict static failures in ductile metallic materials containing different geometrical features. Eng Frac Mech 2008;75:4410-4421.

[22] Susmel L, Taylor D. The theory of critical distances to predict static strength of notched brittle components subjected to mixed-mode loading. Eng Frac Mech 2008;75(3-4):534-550.

[23] Taylor D, Merlo M, Pegley R, Cavatorta MP. The effect of stress concentrations on the fracture strength of polymethylmethacrylate. Mater Sci Eng A 2004;382(1–2):288–294.

[24] Taylor D. Predicting the fracture strength of ceramic materials using the theory of critical distances. Engng Frac Mech 2004;71:2407–2416.

[25] Susmel L, Taylor D. The Theory of Critical Distances to estimate the static strength of notched samples of Al6082 loaded in combined tension and torsion. Part I: Material cracking behaviour. Eng Frac Mech 2010;77:452–469.

[26] Susmel L, Taylor D. The Theory of Critical Distances to estimate the static strength of notched samples of Al6082 loaded in combined tension and torsion. Part II: Multiaxial static assessment. Eng Frac Mech 2010;77:470–478.

[27] Ameri AAH, Davison JB, Susmel L. On the use of linear-elastic local stresses to design load-carrying fillet-welded steel joints against static loading. Eng Frac Mech 2015;136:38-57.

[28] Peterson RE. Notch Sensitivity. In: Sines G, Waisman JL, editors. Metal Fatigue. New York: McGraw Hill; 1959.

[29] Neuber H. Theory of notch stresses: principles for exact calculation of strength with reference to structural form and material. 2nd Edition, Berlin, Germany, Springer Verlag, 1958.

[30] Sheppard SD. Field effects in fatigue crack initiation: long life fatigue strength. Trans ASME J Mech Design 1991;113:188–94.

[31] Bellett D, Taylor D, Marco S, Mazzeo E, Guillois J, Pircher T. The fatigue behaviour of three-dimensional stress concentrations. Int J Fatigue 2005;27:207-221.

[32] Li W, Susmel L, Askes H, Liao F, Zhou T. Ductile fracture of Q460 steel: application of the Theory of Critical Distances. Eng Fail Anal 2016;70:378-389.

[33] Taylor D. The Theory of Critical Distances: A link to micromechanisms. Theor Appl Fract Mec 2017;90:228-233.

[34] Jadallah O, Bagni C, Askes H, Susmel L. Microstructural length scale parameters to model the high-cycle fatigue behaviour of notched plain concrete. Int J Fatigue 2016;82:708–720.

[35] Whitney JM, Nuismer RJ. Stress Fracture Criteria for Laminated Composites Containing Stress Concentrations. J Compos Mater 1974;8(3):253–265.

[36] Susmel L., Taylor D., The Theory of Critical Distances as an alternative experimental strategy for the determination of K_{Ic} and ΔK_{th}. Eng Frac Mech 2010;77:1492–1501.

[37] Yin, T., Tyas, A., Plekhov, O., Terekhina, A., Susmel, L. A novel reformulation of the Theory of Critical Distances to design notched metals against dynamic loading. Mater Des 2015;69:197–212.

[38] Li, W., Askes, H., Susmel, L. Notch failure versus interior failure for mixed-mode in-plane loading. Int. J. Solids Struct., 150, pp. 208-221, 2018.

[39] Reji J., Shah SP. Mixed-mode Fracture of Concrete subjected to Impact Loading. J Struct Eng 1990;116:585–602.

[40] Lambert DE, Ross CA. Strain Rate Effects on Dynamic Fracture and Strength. Int J Impact Eng 2000;24:985–998.

[41] Anon. EN 12390-5:2019 - Testing hardened concrete - Part 5: Flexural strength of test specimens. The British Standards Institution, ISBN 978 0 580 98434 1, 2019.

[42] Karihaloo, BL. Fracture Mechanics and Structural Concrete. Longman Scientific & Technical, London, UK, 1995.

[43] Gómez FJ, Elices M, Berto F, Lazzarin P. Fracture of V-notched specimens under mixed mode (I + II) loading in brittle materials. Int J Fract 2009;159:121.

[44] Lazzarin P, Tovo R. A unified approach to the evaluation of linear elastic stress fields in the neighbourhood of cracks and notches. Int J Fract 1996;78:3-19.

[45] Berto F, Lazzarin P, Wang CH. Three-dimensional linear elastic distributions of stress and strain energy density ahead of V-shaped notches in plates of arbitrary thickness. Int J Fract 2004;127(3):265-282.

[46] Liu M, Gan Y, Hanaor DAH, Liu B, Chen C. An improved semi-analytical solution for stress at round-tip notches. Eng Frac Mech 2015;149:134-143.

[47] Teychenne DC, Franklin RE, Erntroy HC, Hobbs DW, Marsh BK. Design of Normal Concrete Mixes. Construction Research Communications, 2nd Edition, 2010. ISBN-13: 978-1860811722.

[48] Anon. Standard Practice for Making and Curing Concrete Test Specimens in the Laboratory. ASTM Standard C192/C192M, ASTM International, West Conshohocken PA, USA, 2007.

[49] Tada H, Paris PC, Irwin GR. The Stress Analysis Handbook. 2nd Edition, Paris Productions Inc., St. Louis, USA, 1985.

[50] Murakami, Y. Stress Intensity Factors Handbook. Pergamon Press, Oxford, UK, 1987.

[51] Montgomery DC, Peck EA, Vining GG. Introduction to Linear Regression Analysis. 5th Edition, Wiley-Blackwell, Oxford, UK, 2012.

[52] Li Z, Guo W, Kuang Z. Three-dimensional elastic stress fields near notches in finite thickness plates. Int J Solids Struct 2000;37:7617-7631.

[53] Meneghetti G, Susmel L, Tovo R. High-cycle fatigue crack paths in specimens having different stress concentration features. Eng Fail Anal 2007;14(4):656-672.

[54] Kotousov A, Wang CH. Three-dimensional stress constraint in an elastic plate with a notch. Int J Solids Struct 2002;39(16):4311-4326.

List of Captions

Table 1. Summary of the results generated by testing the un-notched specimens under static and dynamic Mode I loading.

Table 2. Summary of the results generated by testing under Mode I and Mixed-Mode I/II static and dynamic loading the specimens containing the sharp notches (r_n=1.3 mm).

Table 3. Summary of the results generated by testing under Mode I and Mixed-Mode I/II static and dynamic loading the specimens containing the intermediate notches (r_n=12.5 mm).

Table 4. Summary of the results generated by testing under Mode I and Mixed-Mode I/II static and dynamic loading the specimens containing the blunt notches (r_n=25 mm).

Figure 1. Notched component subjected to Mode I static loading (a) and the TCD effective stress, σ_{eff}, determined according to the Point Method (b) and the Line Method (c).

Figure 2. Using notched specimens to determined critical distance L for ductile materials (a) and for brittle/quasi-brittle materials (b).

Figure 3. Schematisation of the rule to be used to define the focus-path under Mixed-Mode loading (a) and resulting orientation under pure Mode I loading (b).

Figure 4. Un-notched samples (a); symmetric (b) and asymmetric (c) notched specimens (dimensions in millimetres)

Figure 5. Experimental set-ups used to run Mode I three-point bending tests with ρ=0 (a), Mixed-Mode I/II three-point bending (3PB) with ρ=0.18 (b), and Mixed-Mode I/II four-point bending (4PB) with ρ = 0.3 (c) - dimensions in millimetres.

Figure 6. Examples showing the increase over time of the cross head load, P, measured using a loading cell and the resulting local displacement, Δ_c, under pure Mode I loading (a) as well as under Mixed-Mode I/II loading with ρ=0.3 (b).

Figure 7. Summary of the experimental results generated by testing both the un-notched (a) and the notched specimens (b-j) under Mode I (ρ=0) as well as under Mixed-Mode I/II (ρ=0.18, 0.3) static/dynamic loading.

Figure 8. Examples of cracking behaviour observed in the notched samples tested under Mode I loading as well as under Mixed-Mode loading with ρ=0.18 (b) and with ρ=0.3 (c).

Figure 9. Comparison between estimated orientation of the focus path, θ_c, and orientation of the crack initiation plane, θ_a, measured on the surface of the broken specimens containing blunt (a), intermediate (b), and sharp (c) notches.

Figure 10. Accuracy of the PM and LM in estimating the static/dynamic strength of the notched specimens being tested when variable $\dot{Z}$ is taken equal to $\dot{\Delta}_c$ (a, b) and to $\dot{\varepsilon}_p$ (c, d).

Specimen Code	**Testing Set-up**	**Loading Mode**	**Width** *[mm]*	**Thickness** *[mm]*	**Time to failure** *[s]*	**Failure force** *[kN]*	**Displacement rate**[a] *[mm/s]*
S-P1-I (3PB)	3PB	I	50.1	101.2	24.33	3.39	0.0051
S-P2-I (3PB)			50.0	101.0	23.47	3.49	0.0036
S-P3-I (3PB)			50.9	101.0	23.15	3.06	0.0045
M-P1-I (3PB)			50.6	101.3	0.0243	6.94	5.7666
M-P2-I (3PB)			50.5	101.0	0.0309	6.01	5.8159
M-P3-I (3PB)			50.5	101.0	0.0276	5.04	8.6186
F-P1-I (3PB)			49.5	101.3	0.0218	5.56	23.869
F-P2-I (3PB)			49.8	101.2	0.0166	5.94	20.147
F-P3-I (3PB)			49.7	101.4	0.0184	5.74	20.727

[a]Vertical displacement rate measured at the notch tip using DIC

Table 1. Summary of the results generated by testing the un-notched specimens under static and dynamic Mode I loading.

Specimen Code	Testing Set-up	Loading Mode	Notch depth *[mm]*	Gross width *[mm]*	Thickness *[mm]*	Time to failure *[s]*	Failure force *[kN]*	Displacement rate[(a)] *[mm/s]*
S-S1-I (3PB)	3PB	I	51.0	100.3	100.9	19.4200	3.25	0.0029
S-S2-I (3PB)			51.8	101.3	101.3	17.0300	3.36	0.0018
S-S3-I (3PB)			52.3	102.3	100.6	17.4400	2.76	0.0057
M-S1-I (3PB)			51.4	101.1	102.0	0.0282	5.21	9.0375
M-S2-I (3PB)			51.2	100.8	101.3	0.0297	4.36	9.9544
M-S3-I (3PB)			51.7	101.2	101.1	0.0280	4.82	10.506
F-S1-I (3PB)			51.1	100.9	100.9	0.0121	4.77	17.592
F-S2-I (3PB)			51.4	100.4	100.6	0.0120	4.39	24.926
F-S3-I (3PB)			51.2	100.3	100.7	0.0116	5.62	23.446
S-S1-I/II (3PB)	3PB	I/II	52.0	101.3	100.6	25.8200	7.24	0.0035
S-S2-I/II (3PB)			51.8	101.6	100.4	20.0100	5.79	0.0073
S-S3-I/II (3PB)			49.0	101.0	101.2	24.8700	5.32	0.0033
M-S1-I/II (3PB)			51.8	100.8	101.5	0.0282	9.28	3.9562
M-S2-I/II (3PB)			51.6	101.7	101.3	0.0290	9.37	2.524
M-S3-I/II (3PB)			51.5	100.3	100.9	0.0287	9.26	3.7578
F-S1-I/II (3PB)			51.8	100.6	101.0	0.0135	9.21	14.431
F-S2-I/II (3PB)			51.6	101.7	101.4	0.0113	8.92	25.465
F-S3-I/II (3PB)			51.3	101.9	100.9	0.0145	9.25	16.975
S-S1-I/II (4PB)	4PB	I/II	50.6	100.2	101.5	28.4134	9.98	0.0084
S-S2-I/II (4PB)			50.6	100.7	100.9	32.9130	11.86	0.081
S-S4-I/II (4PB)			50.9	100.9	101.2	32.3030	10.72	0.0092
M-S1-I/II (4PB)			51.7	101.4	101.1	0.0576	21.84	5.8798
M-S2-I/II (4PB)			51.4	101.2	101.5	0.0595	18.00	8.4348
M-S4-I/II (4PB)			50.9	101.6	100.7	0.0527	17.69	6.9353
F-S1-I/II (4PB)			51.4	100.8	100.7	0.0330	18.24	12.58
F-S2-I/II (4PB)			51.4	101.7	100.8	0.0350	16.95	13.296
F-S4-I/II (4PB)			51.8	101.3	101.1	0.0324	15.81	11.819

[(a)]Vertical displacement rate measured at the notch tip using DIC

Table 2. Summary of the results generated by testing under Mode I and Mixed-Mode I/II static and dynamic loading the specimens containing the sharp notches (r_n=1.3 mm).

Specimen Code	Testing Set-up	Loading Mode	Notch depth *[mm]*	Gross width *[mm]*	Thickness *[mm]*	Time to failure *[s]*	Failure force *[kN]*	Displacement rate[(a)] *[mm/s]*
S-I1-I (3PB)	3PB	I	49.2	100.4	100.5	13.3500	2.78	0.006
S-I2-I (3PB)			50.7	101.2	100.7	13.3500	2.96	0.0058
S-I3-I (3PB)			51.1	100.9	100.6	13.3400	3.13	0.0109
M-I1-I (3PB)			50.5	100.5	100.9	0.0222	3.69	11.25
M-I2-I (3PB)			50.3	101.2	101.6	0.0164	4.56	9.1224
M-I3-I (3PB)			49.5	101.6	101.2	0.0181	4.30	5.7606
F-I1-I (3PB)			51.1	101.7	100.9	0.0104	4.53	17.791
F-I2-I (3PB)			49.9	100.6	101.1	0.0084	4.88	19.623
F-I3-I (3PB)			51.9	102.0	101.1	0.0099	4.81	19.676
S-I1-I (3PB)	3PB	I/II	52.7	102.0	101.2	21.0300	6.94	0.0096
S-I2-I (3PB)			50.1	100.9	101.0	23.0800	5.60	0.0121
S-I3-I (3PB)			51.1	100.1	100.8	24.2200	7.08	0.0076
M-I1-I (3PB)			50.4	100.7	101.0	0.0286	8.62	4.7446
M-I2-I (3PB)			50.8	101.6	101.1	0.0229	7.69	5.8804
M-I3-I (3PB)			50.9	100.8	100.8	0.0326	6.94	8.0843
F-I1-I (3PB)			51.2	101.5	100.7	0.0154	10.36	19.692
F-I2-I (3PB)			51.2	101.1	100.3	0.0124	7.73	22.747
F-I3-I (3PB)			51.2	101.5	100.4	0.0152	9.68	19.854
S-I1-I (4PB)	4PB	I/II	51.5	101.4	101.2	38.8000	14.06	0.0111
S-I2-I (4PB)			51.6	102.5	100.5	39.1500	13.08	0.01
S-I4-I (4PB)			52.6	101.2	101.5	39.2500	15.98	0.0084
M-I1-I (4PB)			51.2	101.4	101.4	0.0524	17.89	8.254
M-I2-I (4PB)			50.3	101.2	71.1	0.0523	15.10	6.3663
M-I4-I (4PB)			51.0	101.1	101.2	0.0501	17.95	5.8772
F-I1-I (4PB)			50.8	100.5	100.5	0.0291	19.41	17.376
F-I2-I (4PB)			50.7	100.8	100.9	0.0371	21.79	13.052
F-I4-I (4PB)			50.8	101.1	100.9	0.0286	21.90	18.707

[(a)]Vertical displacement rate measured at the notch tip using DIC

Table 3. Summary of the results generated by testing under Mode I and Mixed-Mode I/II static and dynamic loading the specimens containing the intermediate notches (r_n=12.5 mm).

Specimen Code	Testing Set-up	Loading Mode	Notch depth *[mm]*	Gross width *[mm]*	Thickness *[mm]*	Time to failure *[s]*	Failure force *[kN]*	Displacement rate[(a)] *[mm/s]*
S-B1-I (3PB)	3PB	I	49.6	100.6	100.6	12.7100	3.06	0.0064
S-B2-I (3PB)			50.2	102.3	101.2	15.9500	2.91	0.0116
S-B3-I (3PB)			50.5	100.3	100.6	16.0800	3.24	0.0095
M-B1-I (3PB)			51.8	102.3	101.3	0.0316	4.02	9.4825
M-B2-I (3PB)			50.6	100.3	101.4	0.0186	4.48	7.9204
F-B1-I (3PB)			51.1	100.6	101.1	0.0093	4.71	19.7
F-B2-I (3PB)			50.4	101.2	100.9	0.0102	5.37	22.196
F-B3-I (3PB)			51.2	100.2	101.2	0.0116	5.27	20.324
S-B1-I/II (3PB)	3PB	I/II	50.9	101.3	100.9	31.0700	7.20	0.0065
S-B2-I/II (3PB)			50.3	101.5	100.8	25.0700	7.01	0.0134
S-B3-I/II (3PB)			51.8	100.7	100.4	25.6600	6.64	0.0087
M-B1-I/II (3PB)			50.9	100.7	101.7	0.0257	7.39	5.687
M-B2-I/II (3PB)			50.2	101.3	101.1	0.0286	7.69	4.0413
M-B3-I/II (3PB)			50.9	101.1	100.9	0.0270	8.39	5.5763
F-B1-I/II (3PB)			51.0	100.8	100.6	0.0184	9.00	17.481
F-B2-I/II (3PB)			50.6	101.2	100.8	0.0173	10.38	17.943
F-B3-I/II (3PB)			51.0	101.2	101.2	0.0177	9.49	18.98
S-B1-I/II (4PB)	4PB	I/II	47.3	100.5	101.5	28.7500	10.10	0.0078
S-B2-I/II (4PB)			50.1	101.3	100.5	36.0100	12.55	0.0074
S-B4-I/II (4PB)			50.6	100.0	100.6	32.8100	11.05	0.0085
M-B1-I/II (4PB)			51.4	101.5	101.2	0.0422	12.99	8.9264
M-B2-I/II (4PB)			50.6	101.3	101.6	0.0487	14.29	6.707
M-B4-I/II (4PB)			50.5	100.7	100.7	0.0465	14.62	7.1323
F-B1-I/II (4PB)			51.2	101.6	101.0	0.0289	19.51	17.078
F-B2-I/II (4PB)			49.8	100.7	100.8	0.0264	20.07	15.934
F-B4-I/II (4PB)			49.9	100.5	100.7	0.0324	20.63	17.759

[(a)]Vertical displacement rate measured at the notch tip using DIC

Table 4. Summary of the results generated by testing under Mode I and Mixed-Mode I/II static and dynamic loading the specimens containing the blunt notches (r_n=25 mm).

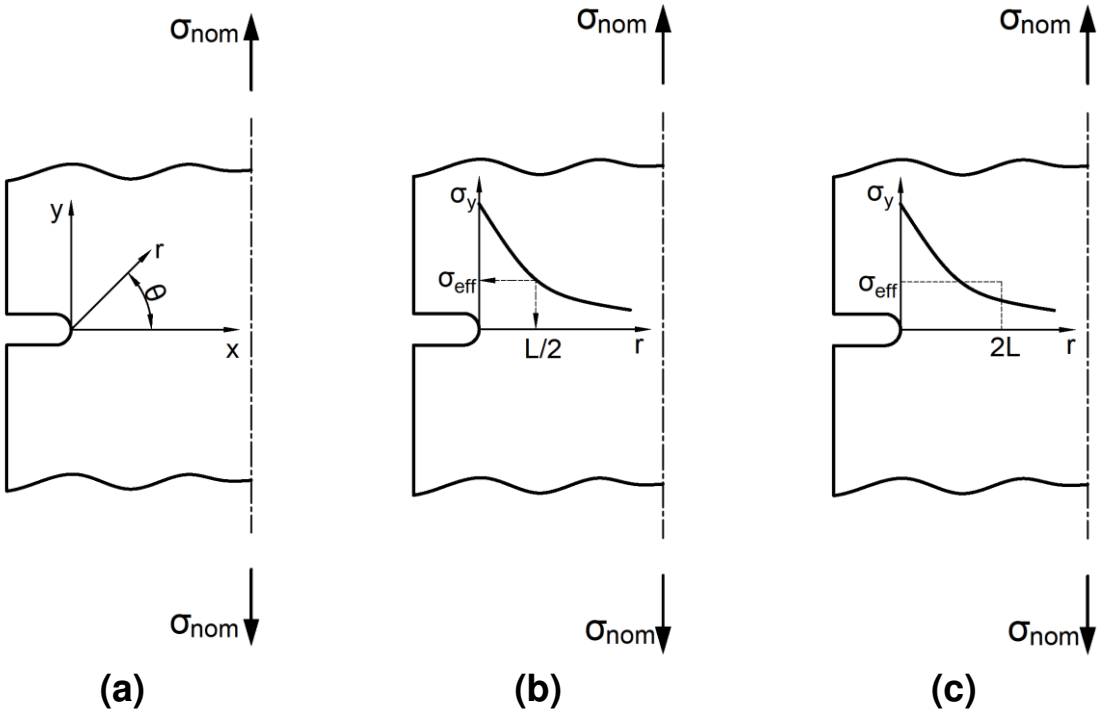

Figure 1. Notched component subjected to Mode I static loading (a) and the TCD effective stress, σ_{eff}, determined according to the Point Method (b) and the Line Method (c).

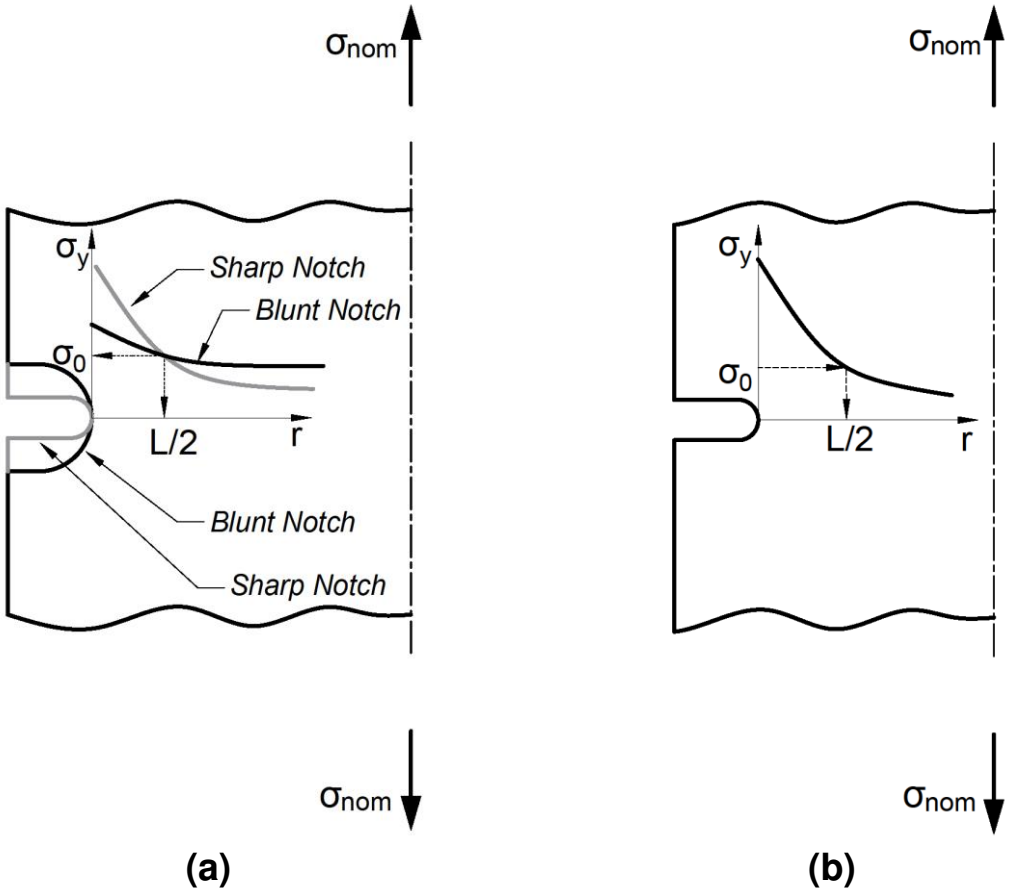

Figure 2. Using notched specimens to determined critical distance L for ductile materials (a) and for brittle/quasi-brittle materials (b).

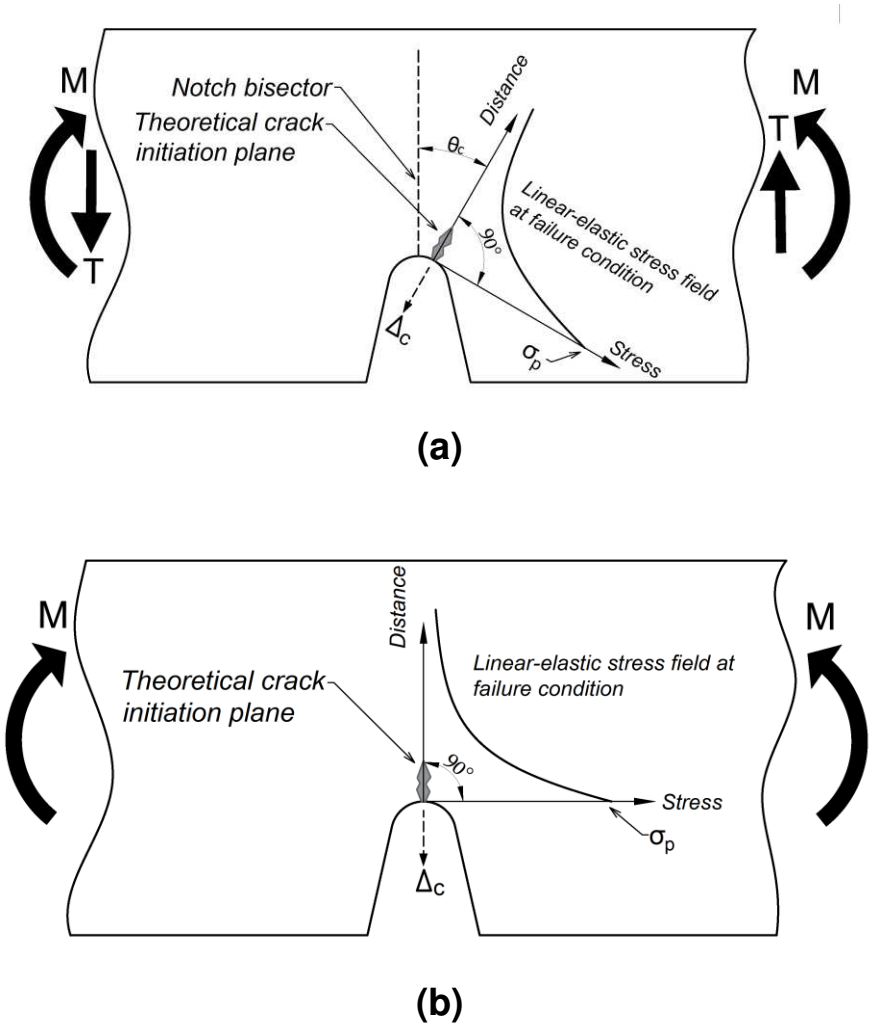

Figure 3. Schematisation of the rule to be used to define the focus-path under Mixed-Mode loading (a) and resulting orientation under pure Mode I loading (b).

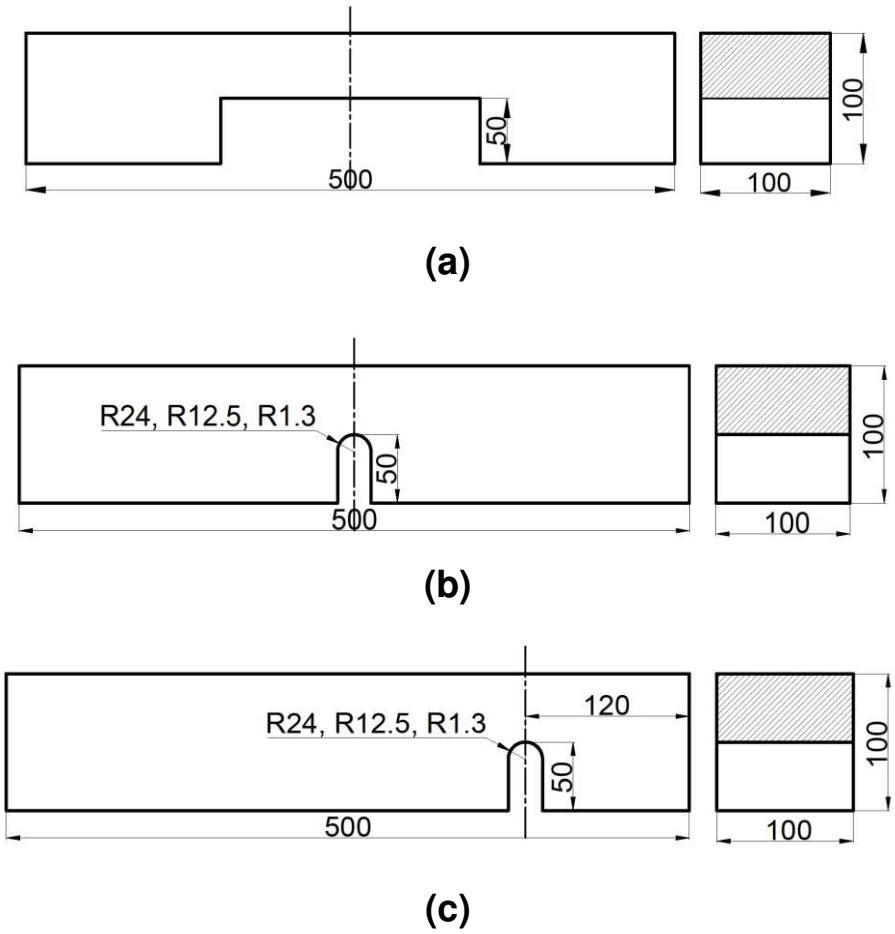

Figure 4. Un-notched samples (a); symmetric (b) and asymmetric (c) notched specimens (dimensions in millimetres)

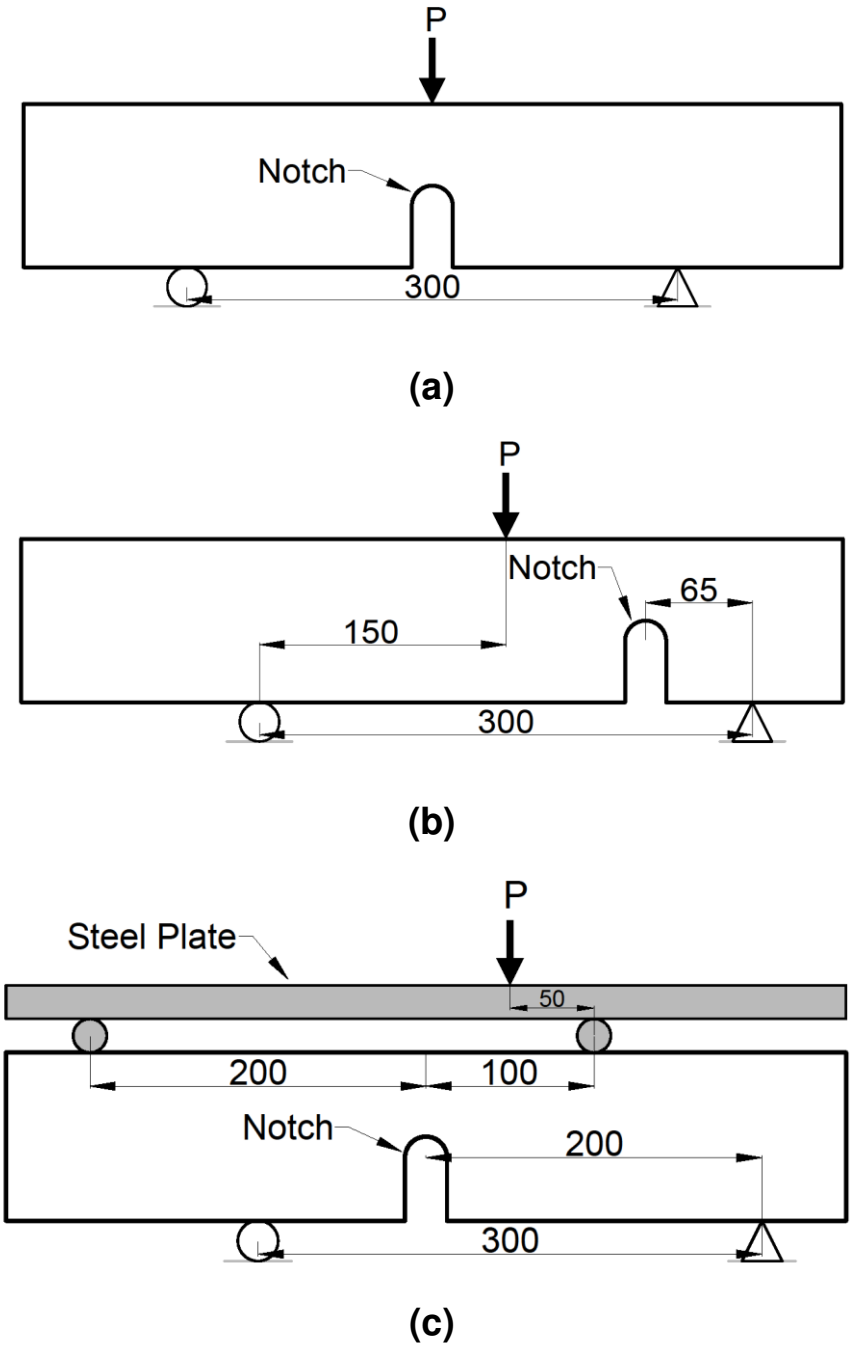

Figure 5. Experimental set-ups used to run Mode I three-point bending tests with ρ=0 (a), Mixed-Mode I/II three-point bending (3PB) with ρ=0.18 (b), and Mixed-Mode I/II four-point bending (4PB) with ρ=0.3 (c) - dimensions in millimetres.

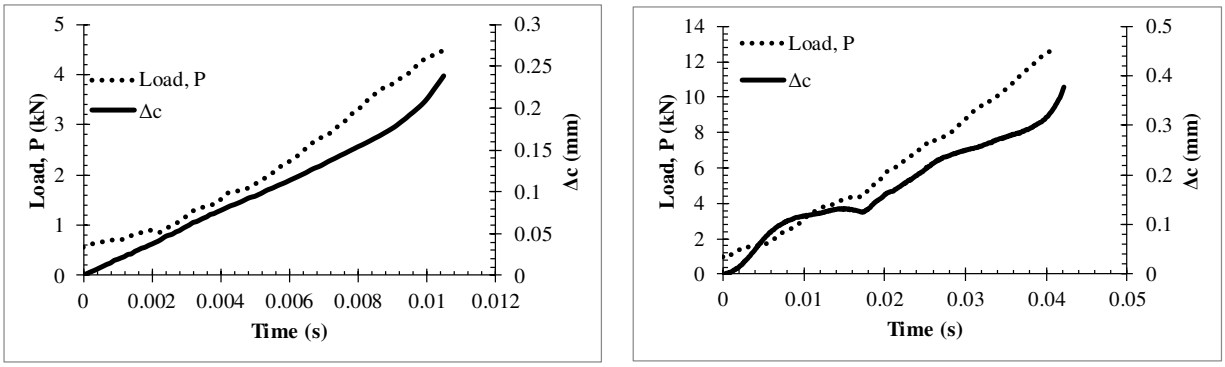

$\dot{\Delta}_c = 20.42\ mm/s$ **(a)**

$\dot{\Delta}_c = 7.40\ mm/s$ **(b)**

Figure 6. Examples showing the increase over time of the cross head load, P, measured using a loading cell and the resulting local displacement, Δ_c, under pure Mode I loading (a) as well as under Mixed-Mode I/II loading with ρ=0.3 (b).

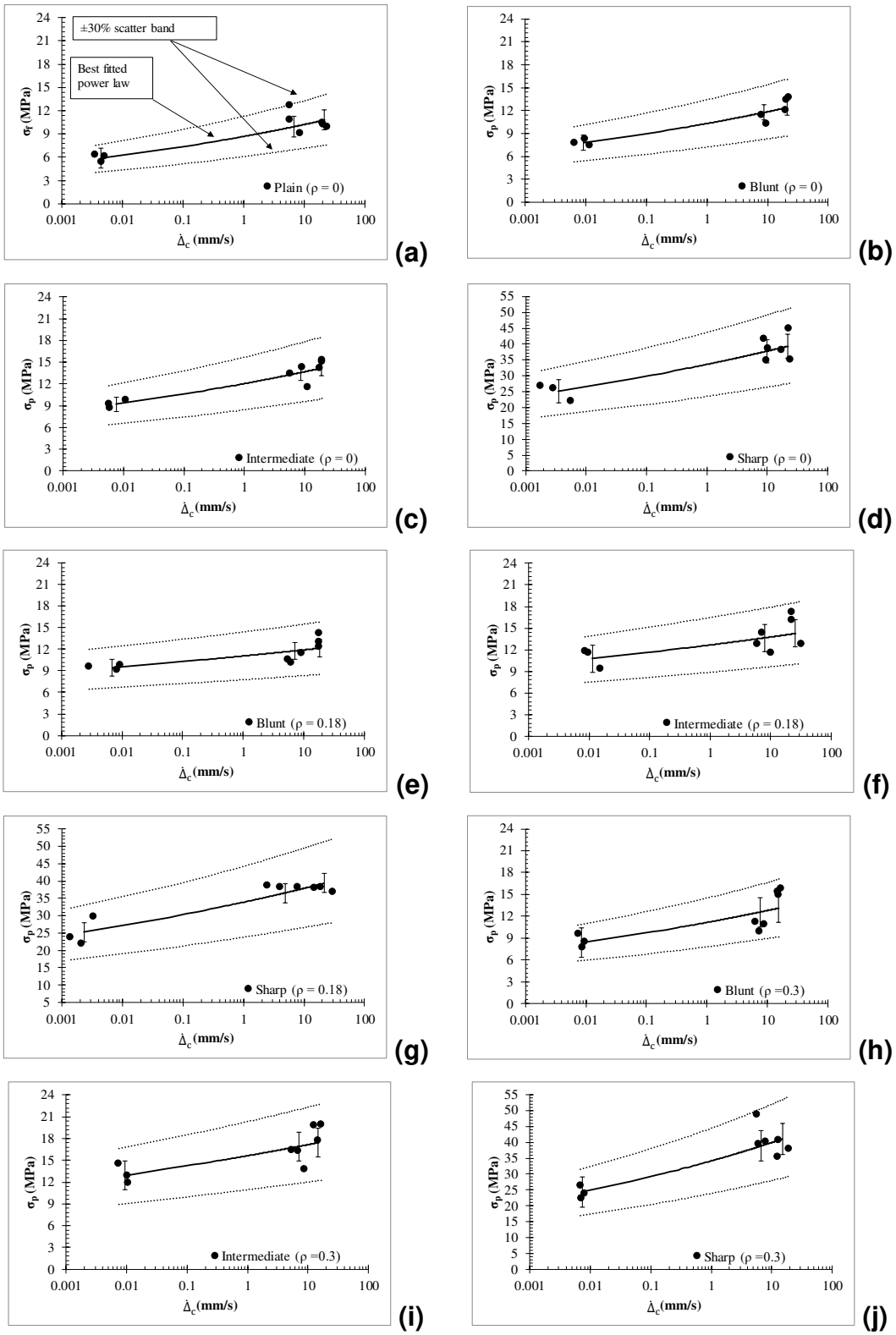

Figure 7. Summary of the experimental results generated by testing both the un-notched (a) and the notched specimens (b-j) under Mode I (ρ=0) as well as under Mixed-Mode I/II (ρ=0.18, 0.3) static/dynamic loading.

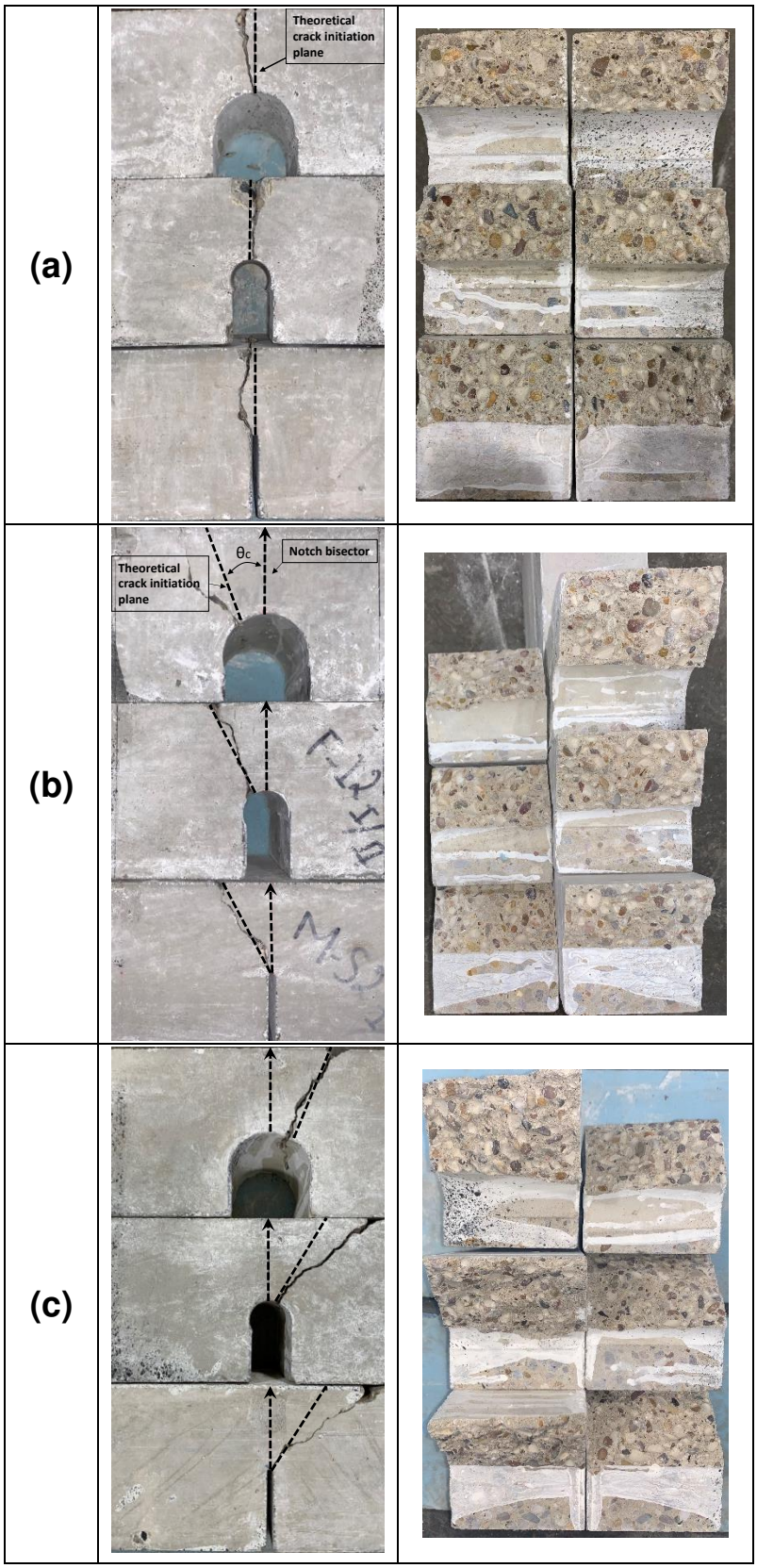

Figure 8. Examples of cracking behaviour observed in the notched samples tested under Mode I loading as well as under Mixed-Mode loading with ρ=0.18 (b) and with ρ=0.3 (c).

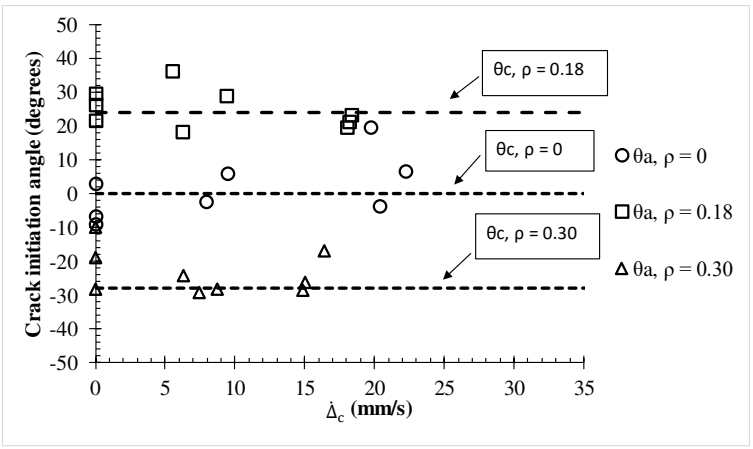

(a)

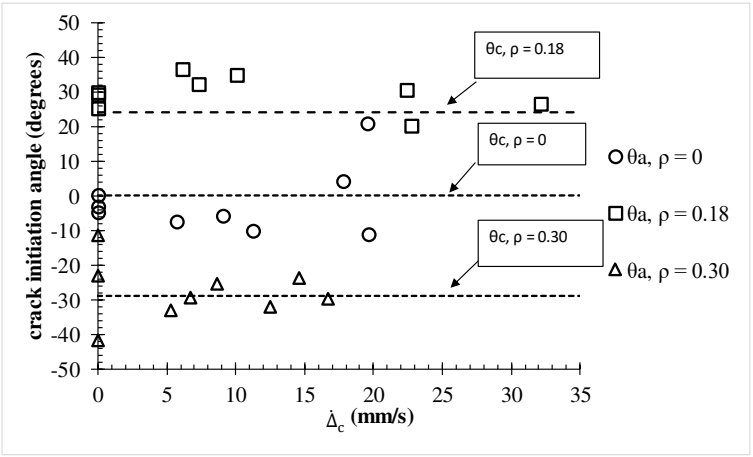

(b)

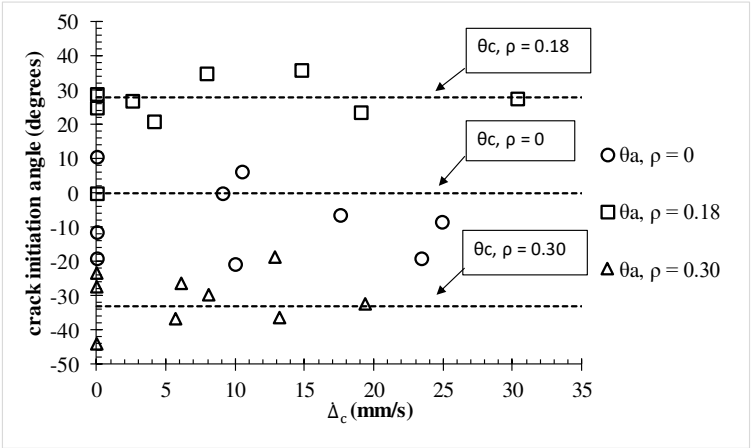

(c)

Figure 9. Comparison between estimated orientation of the focus path, θ_c, and orientation of the crack initiation plane, θ_a, measured on the surface of the broken specimens containing blunt (a), intermediate (b), and sharp (c) notches.

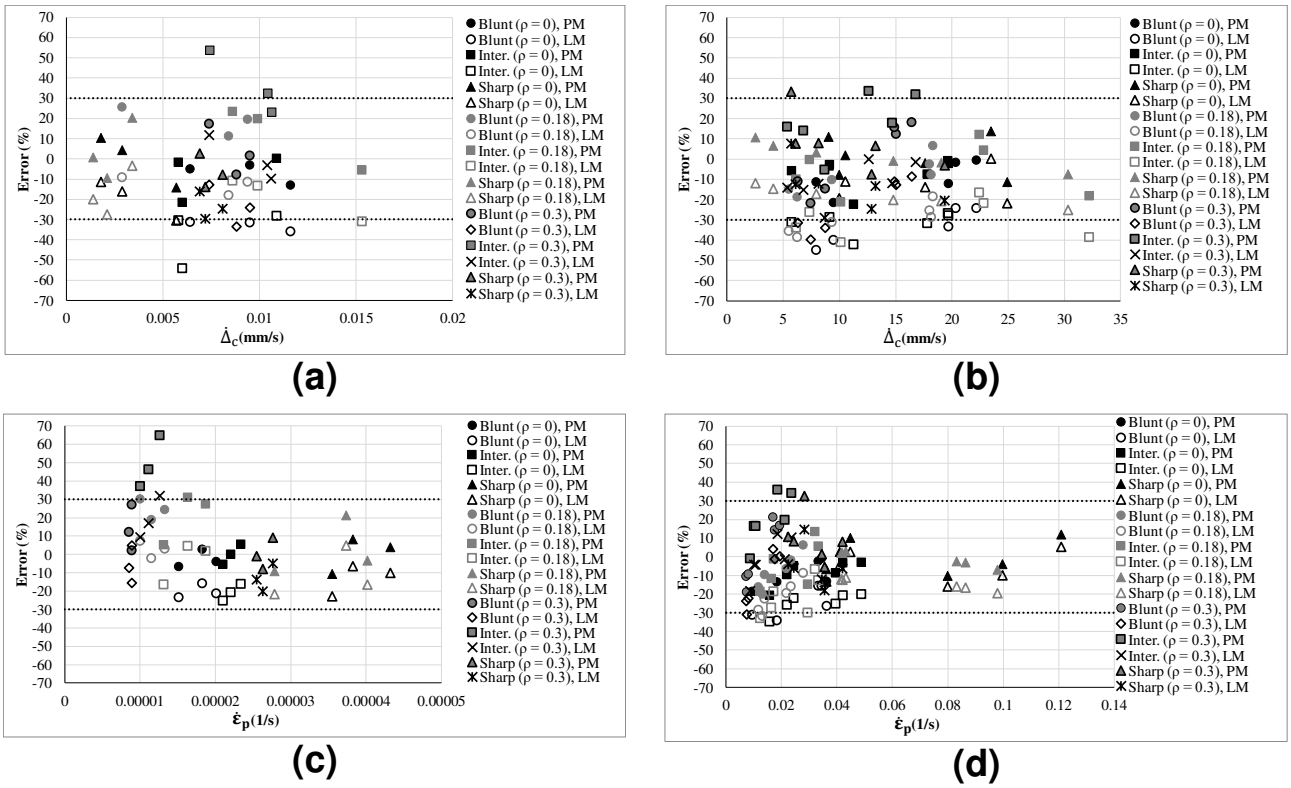

Figure 10. Accuracy of the PM and LM in estimating the static/dynamic strength of the notched specimens being tested when variable $\dot{Z}$ is taken equal to $\dot{\Delta}_c$ (a, b) and to $\dot{\varepsilon}_p$ (c, d).